Comparison of saddle and helical trajectories of a mobile cone beam computed tomography scanner with online calibration correction

Chengtao Wei, Simon Rit, Matthieu Laurendeau, Philipp Steininger, Felix Ginzinger, Marco Riboldi, Christopher Kurz, Guillaume Landry

▶ **To cite this version:**

Chengtao Wei, Simon Rit, Matthieu Laurendeau, Philipp Steininger, Felix Ginzinger, et al.. Comparison of saddle and helical trajectories of a mobile cone beam computed tomography scanner with online calibration correction. Proceedings of the XXth International Conference on the use of Computers in Radiation therapy (ICCR), Jul 2024, Lyon, France. hal-04753338

HAL Id: hal-04753338
https://hal.science/hal-04753338v1

Submitted on 25 Oct 2024

HAL is a multi-disciplinary open access archive for the deposit and dissemination of scientific research documents, whether they are published or not. The documents may come from teaching and research institutions in France or abroad, or from public or private research centers.

L'archive ouverte pluridisciplinaire **HAL**, est destinée au dépôt et à la diffusion de documents scientifiques de niveau recherche, publiés ou non, émanant des établissements d'enseignement et de recherche français ou étrangers, des laboratoires publics ou privés.

Comparison of saddle and helical trajectories of a mobile cone beam computed tomography scanner with online calibration correction

Chengtao Wei[1,2], Simon Rit[3], Matthieu Laurendeau[3,4], Philipp Steininger[5], Felix Ginzinger[5], Marco Riboldi[2], Christopher Kurz[1], and Guillaume Landry[1]

[1]Department of Radiation Oncology, LMU University Hospital, LMU Munich, Munich, Germany
[2]Department of Medical Physics, Ludwig-Maximilians-Universität München, Garching, Germany
[3]Univ Lyon, INSA-Lyon, Université Claude Bernard Lyon 1, UJM-Saint Etienne, CNRS, Inserm, CREATIS UMR 5220, U1294, F-69373 Lyon, France
[4]Thales AVS, Moirans, France
[5]Research & Development, medPhoton GmbH, Salzburg, Austria

Abstract In cone-beam computed tomography (CBCT), the cone-beam (CB) artefact causes object-dependent image distortions away from the central plane. Non-circular trajectories such as saddles or helices can mitigate the CB artefact, but are challenging to execute with scanners not specifically designed for non-circular scanning. In this work, we made use of a recently available mobile robotic CBCT scanner (mobile ImagingRing, medPhoton, Salzburg, Austria) which allows sinusoidal motion perturbation of several degrees of freedoms during a source and detector rotation, coupled with infrared (IR) motion tracking to measure the geometry of each trajectory. We scanned a disk phantom designed to highlight CB artefacts with circular, saddle and helical trajectories executed by driving motion with wheels. We computed an incompleteness metric, $\tan(\psi)$, and correlated it with the region free from CB artefacts in the images. Using a separate cylindrical phantom, we additionally computed the modulation transfer function at 10 percent (MTF_{10}) to assess the accuracy of the calibration correction. We found regions free of CB artefacts of up to 190 mm in the superior-inferior direction for the saddle trajectory, and of 120 mm to 140 mm for the helical trajectory. MTF_{10} was 1.39 lp/mm, 0.98 lp/mm and 1.03 lp/mm for the circular, saddle and helical trajectories with IR tracking, while without IR tracking the saddle and helical trajectories had MTF_{10} less than 0.4 lp/mm.

1 Introduction

In cone-beam computed tomography (CBCT), non-circular scanning trajectories can eliminate the well known cone-beam (CB) artefact, which stems from data incompleteness when moving away from the plane containing the source trajectory. For points away from that plane, Tuy's condition is not satisfied since there will always be planes through these points which do not intersect the trajectory [1]. This issue can reduce image quality in a wide range of medical imaging applications, including dentistry, image-guided surgery and image-guided radiotherapy. The degree of incompleteness can be quantified with the $\tan(\psi)$ metric introduced by Clackdoyle et al. [2], which provides a continuous value which was shown to correlate with the severity of the CB artifact [3]. It is well known that using non-circular trajectories in CBCT scanning can mitigate the CB artifact, with publications demonstrating sinusoidal trajectories [4–6], circle-and-line or circle-and-arc trajectories [7, 8], or even freely optimized trajectories [9–11]. While several works have demonstrated improvements from such trajectories, often they have been performed at devices not specifically designed for such a purpose, entailing complex trajectory programming or long scanning times. Recently, a mobile robotic CBCT scanner (mobile ImagingRing, medPhoton GmbH, Salzburg, Austria) has become available with the option to execute sinusoidal perturbations along various axes of motion. This allows implementing time-efficient non-circular trajectories which can be executed with one rotation of the source and detector, such as saddle [12] and helical [13, 14] trajectories. The device is further equipped with infrared (IR) tracking technology which allows mitigating geometric inaccuracies in recorded trajectories, which can degrade spatial resolution. In this work we compared CB artefact reduction achievable with saddle and helical trajectories using scans of a disk phantom and $\tan(\psi)$ evaluation, in addition to modulation transfer function at 10 percent (MTF_{10}) analysis with a separate phantom.

2 Materials and Methods

2.1 Mobile robotic CBCT scanner and trajectories

All CBCT scans were acquired at the mobile robotic CBCT scanner described in Figure 1 and equipped with IR tracking based on a pair of cameras which monitor the position of a tracking object placed on the phantoms (Rigid Body Marker Base, MCP1145; NaturalPoint, Inc., Corvallis, USA). The scanner's motorized wheels allowed the execution of saddle and helical trajectories. For the saddle trajectory, a rotation with angle β around a vertical yaw rotation axis, which is displayed in Figure 1, was performed during source and detector rotation, expressed with rotation angle θ, according to

$$\beta(\theta) = A_{\text{saddle}} \sin(\omega_{\text{saddle}}\theta + \phi_{\text{saddle}}) \quad (1)$$

where A_{saddle}, ω_{saddle} and ϕ_{saddle} are the amplitude, the angular frequency and the phase shift of the yaw perturbation. For the helical trajectory a similar sinusoidal perturbation D displacing the scanner longitudinally in the superior-inferior (SI) direction followed

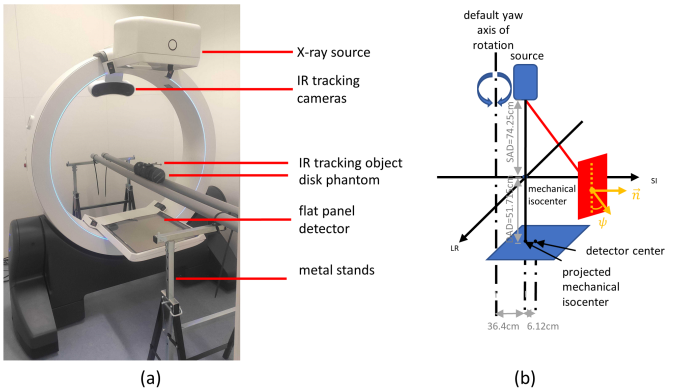

Figure 1: Setup and geometrical information of the CBCT scanner. (a) The whole setup for the experiments (note that the plastic support was replaced by a carbon fiber table). IR tracking markers are put on the phantom to be visible by both tracking cameras. (b) Basic geometrical information of the CBCT scanner and the rotation axis and source projection offset relative to the detector center. The geometry used to calculate $\tan(\psi)$ is shown in red and orange (see Ref [2] for details).

Table 1: Parameters of the saddle and helical trajectories defined by equations 1 and 2 with θ expressed in rad. A_{saddle} is expressed in degrees for clarity.

A_{saddle} [°]	ω_{saddle} [rad^{-1}]	ϕ_{saddle} [rad]	A_{helical} [cm]	ω_{helical} [rad^{-1}]	ϕ_{helical} [rad]
10	1	π	7.7	0.5	$\frac{\pi}{2}$

$$D(\theta) = A_{\text{helical}} \sin(\omega_{\text{helical}}\theta + \phi_{\text{helical}}) \quad (2)$$

where A_{helical}, ω_{helical} and ϕ_{helical} are the amplitude, the angular frequency and the phase shift of the longitudinal perturbation. The values used in this work are listed in Table 1.

The IR tracking system provided the position and direction of the rigid object for each projection, which were transformed into a rotation matrix R and translation t. The recorded source position s, detector position d and orthogonal detector direction vectors u and v (in the gantry's coordinate system) were transformed as follows to account for the perturbations executed following equations 1 and 2.

$$\begin{aligned} s' &= R_0 R^{-1}(s-t) + t_0, \\ d' &= R_0 R^{-1}(d-t) + t_0, \\ u' &= R_0 R^{-1} u, \\ v' &= R_0 R^{-1} v, \end{aligned} \quad (3)$$

where R_0 and t_0 are for the first frame and R and t for the current frame.

2.2 Phantoms, experiments and simulations

Two phantoms were used in this work. The first was a disk phantom consisting of eleven 1 mm thick acrylic disks of 100 mm diameter separated by 20 mm foam spacers, which was used to assess CB artefacts. The second was an acrylic cylinder of 152 mm diameter used to evaluate MTF_{10}. Both phantoms were scanned using circular, saddle and helical trajectories acquiring 720 projections with θ ranging from 0 to 2π, exposure of 20 ms and 5 mA and with IR tracking enabled. The detector was 432 mm $\times$ 432 mm with 1440 pixels $\times$ 1440 pixels. The geometrical information from equation 3 was additionally used to simulate a digitally reconstructed radiograph (DRR) for each projection of the disk phantom, using a digital voxelized version of the phantom with a voxel size of 0.5 mm^3. This was done using functions from the Reconstruction Toolkit (RTK) software package (version 2.3.0) [15].

2.3 Image reconstruction

All images were reconstructed using RTK. We used penalized least-squares minimization with the conjugate gradient algorithm with a regularization weight of $\gamma = 10$, a voxel size of 0.5 mm^3 and 50 iterations. We reconstructed all experimental and simulated acquisitions defined above.

2.4 Image analysis

For each experimental acquisition, the incompleteness metric $\tan(\psi)$ was calculated according to Clackdoyle et al. [2] for all positions in the reconstructed image. The value of $\tan(\psi)$ is 0 for complete data and has been shown to allow adequate reconstruction up to 0.02 [16], above which conspicuous CB artefacts can be expected. In more detail, for all the projection lines passing through a voxel, we calculated and kept those projection lines that fell on the detector, following the approach of Sun et al. [16]. Then, for one specific direction $\vec{n}$, we took the lowest $\tan(\psi)$ from all the source positions. Finally, we took the largest $\tan(\psi)$ value from all directions as the incompleteness value for this voxel. Here, ψ was the angle between the plane and the projection line. The red and orange parts of Figure 1(b) show the geometry of this calculation. For the saddle and helical trajectories, we quantified the extent of the region free from CB artefacts based on visual inspection and overlaid $\tan(\psi)$ isolines.

The MTF_{10} was calculated using an over-sampled edge obtained from the cylindrical phantom's outer diameter and was used to determine the performance of IR tracking. This was done slice-by-slice for an SI region of 100 mm and we calculated the mean and standard deviation of MTF_{10}. Comparison of simulations and experiments was used to determine whether potential image distortions stemmed from the trajectories themselves or from issues with IR tracking.

3 Results

Figure 2 shows the source trajectories performed in experiments. All the trajectories started at 0 mm in SI, the saddle

trajectory extended to −135 mm, and the helical trajectory extended to −154 mm in SI. The source executed a single rotation around the gantry for all the trajectories. Table 2 reports the MTF_{10} for the circular, saddle, and helical trajectories. The spatial resolution was the same for the circular trajectory with and without IR tracking. The spatial resolution of the saddle and helical trajectory both had important improvements when using IR tracking correction. The spatial resolution was improved from 0.37 mm to 0.98 mm for the saddle trajectory and from 0.34 mm to 1.03 mm for the helical trajectory.

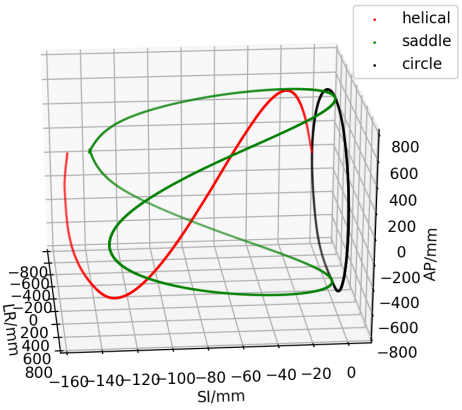

Figure 2: The three trajectories used in this work. The black line represents the circular trajectory, the green line is the yaw-based saddle trajectory, and the red line is the helical trajectory. Axes not to scale.

Table 2: MTF_{10} for different trajectories w/ and w/o IR tracking (mean ± standard deviation).

	with IR tracking	**w/o IR tracking**
	[lp/mm]	
circle	1.39 ± 0.06	1.39 ± 0.04
saddle	0.98 ± 0.07	0.37 ± 0.04
helical	1.03 ± 0.09	0.34 ± 0.01

The reconstructed images from the simulations of the three trajectories are shown in Figure 3. The disks inside the low incompleteness region ($\tan(\psi) < 0.02$) are all well reconstructed without CB artifacts and distorted into spindle shapes when lying outside of the low incompleteness region. For the saddle trajectory, the shape of the low incompleteness region was an irregular cylinder with 190 mm height in SI and a cross-section which had a short axis of 255 mm and a long axis of 270 mm. For the helical trajectory, the low incompleteness region had a round cross-section with diameter 255 mm, while the height in SI ranged from 120 mm to 140 mm as shown in Figure 3 (c).

Figure 4 shows the coronal plane of the reconstructed images from the experimental acquisitions with the three trajectories,

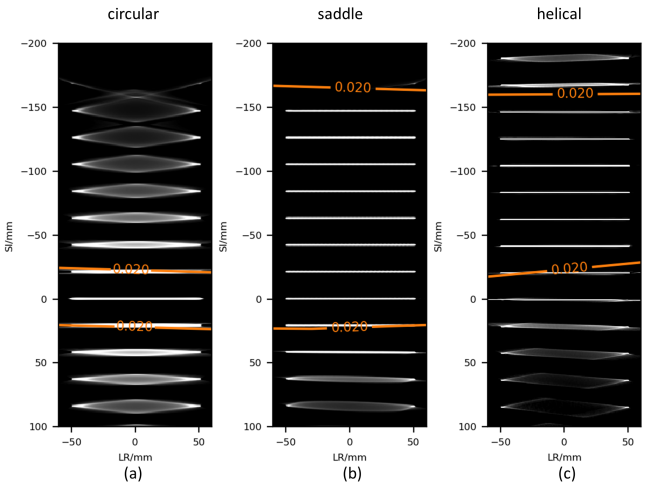

Figure 3: Reconstructed images of the digital disk phantom from the three simulated trajectories in a superior-inferior (IR) and left-right (LR) view. Orange lines indicate the edges of the low incompleteness region where $\tan(\psi) < 0.02$.

with convex hull and incompleteness overlays. The sizes and shapes of the low incompleteness regions are the same as the simulation, and whithin all disks are well reconstructed. We could confirm the observation from the simulation that the saddle trajectory provided a larger region where disks are well reconstructed. We can observe that the low incompleteness region is larger than the convex hull for all trajectories.

4 Discussion

Table 2 and Figure 4 show that the IR tracking correction is reliable and can provide accurate geometrical corrections online. The MTF_{10} of the saddle and the helical trajectories with IR tracking, although lower than for the circular scan, were comparable to that achievable at a linac-mounted CBCT scanner (XVI, Elekta, UK), for which we measured a MTF_{10} of 1.00 ± 0.01 lp/mm with a circular scan. Both the simulation (Figure 3) and the experiment (Figure 4) show that the helical trajectory provides a longer reconstructed region where more disks than for the saddle scan could be reconstructed, albeit in a distorted fashion. However, the low incompleteness region of the helical trajectory was smaller in SI than that of the saddle trajectory, despite the source having moved a larger distance along the SI direction for the helical trajectory. This was attributed to the non-closed nature of the trajectory, and helical trajectory simulations demonstrated that using $\omega_{\text{helical}} = 2\,\text{rad}^{-1}$ could provide a convex hull with an SI extent corresponding to $2A_{\text{helical}}$. We can also see in Figure 3 that at least one disk outside of the low incompleteness region is well reconstructed. These observations suggest that the SI length of the low incompleteness region is limited by a direction $\vec{n}$ other than that normal to the disks. One advantage of the helical trajectory over the saddle was that it was less likely to collide with the patient couch, which might occur when performing saddle trajectories with larger A_{saddle}.

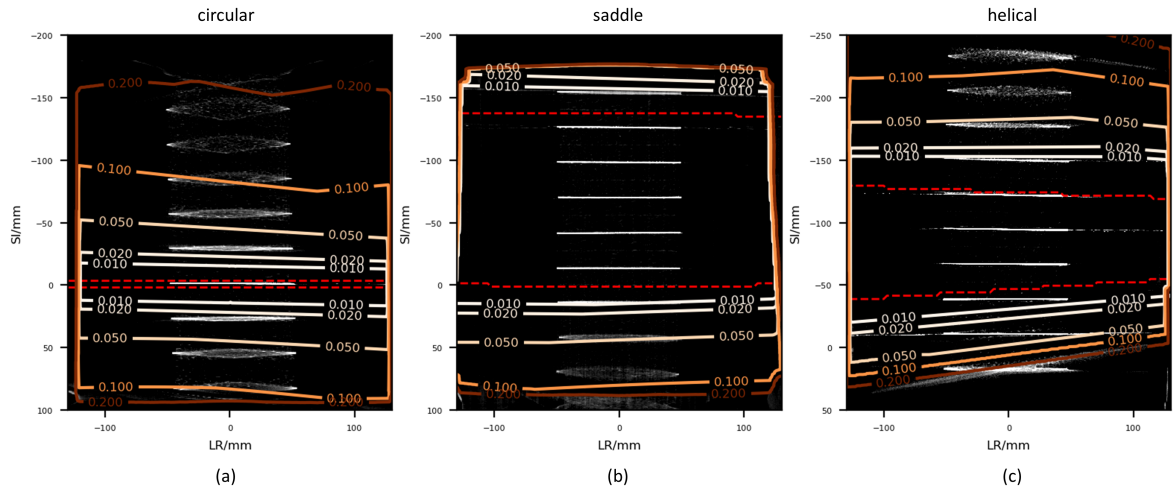

Figure 4: Reconstructed images of the disk phantom from experimental trajectories in a superior-inferior (IR) and left-right (LR) view, with convex hull and $\tan(\psi)$ isolines overlay. Red dashed lines are edges of the convex hull and the solid lines are $\tan(\psi)$ isolines.

5 Conclusion

In conclusion, both the yaw-based saddle and helical trajectories were feasible with online IR tracking geometrical corrections at the mobile robotic CBCT scanner used in this work. This allowed an important increase of the low incompleteness region ($\tan(\psi) < 0.2$) and elimination of the CB artifact.

References

[1] H. K. Tuy. "An Inversion Formula for Cone-Beam Reconstruction". *SIAM Journal on Applied Mathematics* 43.3 (1983), pp. 546–552.

[2] R. Clackdoyle and F. Noo. "Quantification of Tomographic Incompleteness in Cone-Beam Reconstruction". *IEEE Transactions on Radiation and Plasma Medical Sciences* 4.1 (Jan. 2020), pp. 63–80. DOI: 10.1109/TRPMS.2019.2918222.

[3] A. Tersol, P. Wu, R. Clackdoyle, et al. "Sampling effects for emerging cone-beam CT systems and scan trajectories: from Tuy's condition to system design and routine image quality tests". en. *Medical Imaging 2022: Physics of Medical Imaging*. Ed. by W. Zhao and L. Yu. San Diego, United States: SPIE, Apr. 2022, p. 55. DOI: 10.1117/12.2613139.

[4] Y. Q. Ma, G. J. Gang, T. Ehtiati, et al. "Non-Circular CBCT Orbit Design and Realization on a Clinical Robotic C-arm for Metal Artifact Reduction". *Medical Imaging 2022: Image-Guided Procedures, Robotic Interventions, and Modeling*. Ed. by C. A. Linte and J. H. Siewerdsen. San Diego, United States: SPIE, Apr. 2022, p. 8. DOI: 10.1117/12.2612448.

[5] H. Hosoo, Y. Ito, A. Marushima, et al. "Image Quality Improvements for Brain Soft Tissue in Neuro-Endovascular Treatments: A Novel Dual-Axis "Butterfly" Trajectory for Optimized Cone-Beam CT". *European Journal of Radiology* 160 (Mar. 2023), p. 110713. DOI: 10.1016/j.ejrad.2023.110713.

[6] T. Reynolds, Y. Ma, T. Wang, et al. "Revealing Pelvic Structures in the Presence of Metal Hip Prothesis via Non-Circular CBCT Orbits". *Proceedings of SPIE–the International Society for Optical Engineering* 12466 (Feb. 2023), 124660Y. DOI: 10.1117/12.2652980.

[7] A. Katsevich. "Image reconstruction for the circle and line trajectory". *Physics in Medicine and Biology* 49.22 (Nov. 2004), pp. 5059–5072. DOI: 10.1088/0031-9155/49/22/003.

[8] A. Katsevich. "Image reconstruction for the circle-and-arc trajectory". en. *Physics in Medicine and Biology* 50.10 (May 2005), pp. 2249–2265. DOI: 10.1088/0031-9155/50/10/005.

[9] G. J. Gang, J. H. Siewerdsen, and J. W. Stayman. "Non-circular CT orbit design for elimination of metal artifacts". en. *Medical Imaging 2020: Physics of Medical Imaging*. Ed. by H. Bosmans and G.-H. Chen. Houston, United States: SPIE, Mar. 2020, p. 79. DOI: 10.1117/12.2550203.

[10] J. W. Stayman, S. Capostagno, G. J. Gang, et al. "Task-driven source–detector trajectories in cone-beam computed tomography: I. Theory and methods". en. *Journal of Medical Imaging* 6.02 (May 2019), p. 1. DOI: 10.1117/1.JMI.6.2.025002.

[11] P. Wu, N. Sheth, A. Sisniega, et al. "C-arm orbits for metal artifact avoidance (MAA) in cone-beam CT". en. *Physics in Medicine and Biology* 65.16 (Aug. 2020), p. 165012. DOI: 10.1088/1361-6560/ab9454.

[12] J. D. Pack, F. Noo, and H. Kudo. "Investigation of saddle trajectories for cardiac CT imaging in cone-beam geometry". en. *Physics in Medicine and Biology* 49.11 (June 2004), pp. 2317–2336. DOI: 10.1088/0031-9155/49/11/014.

[13] F. Noo, J. Pack, and D. Heuscher. "Exact helical reconstruction using native cone-beam geometries". en. *Physics in Medicine and Biology* 48.23 (Dec. 2003), pp. 3787–3818. DOI: 10.1088/0031-9155/48/23/001.

[14] H. Yu and G. Wang. "Studies on artifacts of the Katsevich algorithm for spiral cone-beam CT". en. *Developments in X-Ray Tomography IV*. Ed. by U. Bonse. Denver, CO, Oct. 2004, p. 540. DOI: 10.1117/12.559286.

[15] S. Rit, M. V. Oliva, S. Brousmiche, et al. "The Reconstruction Toolkit (RTK), an open-source cone-beam CT reconstruction toolkit based on the Insight Toolkit (ITK)". *Journal of Physics: Conference Series* 489.1 (Mar. 2014), p. 012079. DOI: 10.1088/1742-6596/489/1/012079.

[16] T. Sun, R. Clackdoyle, J.-H. Kim, et al. "Estimation of Local Data-Insufficiency in Motion-Corrected Helical CT". en. *IEEE Transactions on Radiation and Plasma Medical Sciences* 1.4 (July 2017). rate: 2, pp. 346–357. DOI: 10.1109/TRPMS.2017.2710237.